Real-time observation of twinning-detwinning in shock-compressed magnesium via time-resolved *in situ* synchrotron XRD experiments

Cyril L. Williams ◉,[1,*] Chaitanya Kale,[2] Scott A. Turnage,[1] Logan S. Shannahan,[1] Bin Li,[3] Kiran N. Solanki ◉,[2]
Richard Becker,[1] Todd C. Hufnagel,[4] and Kaliat T. Ramesh ◉[5]

[1]*Impact Physics Branch, US Army Research Laboratory, APG, Maryland 21005, USA*
[2]*School for Engineering of Matter, Transport and Energy, Arizona State University, Tempe, Arizona 85287, USA*
[3]*Department of Chemical and Materials Engineering, University of Nevada, Reno, Nevada 89557, USA*
[4]*Department of Materials Science and Engineering, The Johns Hopkins University, Baltimore, Maryland 21218, USA*
[5]*Department of Mechanical Engineering, The Johns Hopkins University, Baltimore, Maryland 21218, USA*

Both engineered and natural materials may be subjected to extremes of elevated pressure, temperature, and strain rate due to shock loading; examples include ballistic impact of projectiles on armor, planetary impacts, and high-speed machining operations. Experimental techniques for ascertaining the macroscopic response of materials to shock loading are well established, but insight into fundamental mechanisms of deformation requires the ability to characterize the evolution of microstructure in real time. Experiments in which specimens are recovered and characterized after shock loading have been widely used to understand structure-property relationships. But these shock recovery experiments only reveal information at the end state of the material, from which the evolution of the structure during unloading must be inferred. There is always the possibility that the structure of the material continues to evolve during unloading, leading to a potential misunderstanding of the structural evolution during shock compression and release. In this paper we describe the results of shock recovery and time-resolved *in situ* x-ray diffraction studies of deformation twinning in an extruded fine-grained AMX602 magnesium alloy. The samples were shock compressed along the plate normal and extrusion directions, then released back to ambient conditions. Analysis of the microstructure before and after shock loading indicates a substantial change in crystallographic texture reflecting substantial deformation twinning. Texture evolution from *in situ* synchrotron x-ray diffraction measurements show significant twinning during shock compression followed by detwinning during stress release. These results not only provide insight into the complex twinning-detwinning behavior of this particular alloy, but also illustrate the utility of *in situ* characterization for bridging the knowledge gap between shock recovery experiments and the transient behavior of materials during shock loading more generally.

I. INTRODUCTION

Modern-day structure-property relationships concerning shock-compressed solids have been studied via shock recovery experiments for more than 60 years dating back to the pioneering research and subsequent seminal paper by Smith in 1958 [1]. They have since been proven to be critical for studying the residual structure-property relationships in condensed matter at the extremes [2–5]. However, a knowledge gap exists between the ambient state (unshocked) and end state (full release), which has plagued the shock compression science community since the inception of shock recovery experiments. Shock recovery experiments do not provide any real-time information on the microstructure between the ambient and end states. This gap in knowledge is extremely crucial in developing a fundamental understanding of the deformation mechanisms active during shock compression and release, and their role on the consequent failure of the

material. The current state-of-the-art approach to bridging this knowledge gap is through time-resolved *in situ* synchrotron x-ray diffraction (XRD) shock experiments and multiscale modeling.

Time-resolved *in situ* synchrotron x-ray diffraction shock experiments provide the ability to probe the dynamic elastic-plastic response of materials in real time while the material is in a known uniaxial strain state. Although their execution is nontrivial, *in situ* synchrotron XRD experiments when synchronized with shock wave profile measurements can provide the necessary information required to bridge the existing knowledge gap in materials under extreme dynamic environments, such as high velocity ballistic impacts, planetary impacts, and explosions. For instance, Turneaure *et al.* [6] recently employed time-resolved *in situ* synchrotron x-ray diffraction shock experiments to study the response of single crystal magnesium shock compressed along the *c* axis. They observed dislocation slip during shock compression and significant twinning during stress release. A similar approach was used to study shock wave driven twinning and lattice dynamics in shock-compressed tantalum for stresses ranging

*Corresponding author: cyril.l.williams.civ@mail.mil

from 10 to 300 GPa [7,8] and to examine the structure of fused silica shock compressed up to 63 GPa [9].

A large volume of research describing the mechanical behavior of magnesium (Mg) and its alloys at low to intermediate strain rates have shown that the two dominant deformation mechanisms are dislocation slip and mechanical twinning [10–17]. When Mg is plastically deformed, the slip systems that are activated strongly depend on the loading direction with respect to the crystallographic orientation and the temperature at which the material is deformed [18–24]. During plastic deformation, Mg offers three possible dislocation Burgers vectors which can be operative on different slip planes; (1) basal slip—the Burgers vector **b** equals $\langle a \rangle = \frac{1}{3}\langle 11\bar{2}0 \rangle$ on the basal (0002) slip plane [12,25], (2) prismatic slip—the Burgers vector **b** equals $\langle a \rangle = \frac{1}{3}\langle 11\bar{2}0 \rangle$ or $c = [0001]$ on the $\{10\bar{1}1\}$ slip plane [12,21,26], and (3) pyramidal slip—the Burgers vector **b** equals $\langle c + a \rangle = \frac{1}{3}\langle 11\bar{2}3 \rangle$ on the slip planes $\{11\bar{2}2\}$ and/or $\{10\bar{1}1\}$ [12,20,27]. The critical resolved shear stress (CRSS) for basal slip with $\langle a \rangle$ dislocation in magnesium has been reported to be approximately 0.5 MPa [10], while the CRSS reported for prismatic and pyramidal dislocations are one to two orders of magnitude higher [10,26,28]. Compared to their face and body centered cubic lattice counterparts, the number of easy slip systems in Mg are limited, therefore, deformation twinning is crucial in accommodating the *c*-axis strain in Mg when plastically deformed [16,29]. The $\{10\bar{1}2\}$ extension twins are dominant and $\{10\bar{1}1\}$ contraction twins are activated at high strains close to fracture [30–33]. Although the mechanical behavior of Mg at low to intermediate strain rates cannot be directly compared to that of shock-compressed Mg and Mg alloys, they do share some similarities. Hence, knowledge acquired from nonshock experiments can provide a background for studying the deformation mechanisms active under shock compression. For instance, compression along the $\langle a \rangle$ axis activates extension twins at all strain rates [11,34,35] but on the other hand, compression along the $\langle c \rangle$ axis can activate contraction twins at low to intermediate strain rates [36] and shock compression [3] if the stress is high enough.

It has been suggested that twinning becomes increasingly difficult as grain size decreases, but is favored at high strain rates [37]. For $\{10\bar{1}2\}$ extension twinning, it can still be activated in ultrafine-grained Mg samples at dynamic strain rates [34,38]. Thus, the motivation for this research is twofold, on one hand we seek to show the feasibility of twinning in shock-compressed fine grained (FG) structures and, on the other hand, we seek to elucidate the results shown in Fig. 1. Figures 1(a1), 1(a2), and 1(a3) are the grain orientation map, pole figure, and grain size distribution, respectively, of the as-received FG extruded AMX602 magnesium plate. Note that the designations ND, ED, and TD used in Fig. 1 represent the plate normal, extrusion, and transverse directions, respectively. The as-received FG material has an average grain size of 3.41 μm and shows a typical extrusion texture with split basal poles; the $\langle c \rangle$ axes are mainly distributed perpendicular about the extrusion direction [see Fig. 1(a2)]. When shock compressed along the plate normal to approximately 3 GPa and then soft recovered, the results from Figs. 1(b1), 1(b2),

and 1(b3) reveal a 25% increase in grain size, from 3.41 to 4.27 μm perhaps due to temperature effects. It is evident from Fig. 1(b2) that the majority of the basal poles have been reoriented by approximately 90° about the plate normal suggestive of $\{10\bar{1}2\}$ extension twinning. Similar behavior has been observed in extruded AZ31 magnesium alloy at lower strain rates by Kada [39]. Compounded by this complex behavior is the fact that the twin volume fraction of the as-received and shock recovered samples computed as the area fraction of the twins on the electron backscatter diffraction (EBSD) maps shown in Figs. 1(a1) and 1(b1) were approximately 0% and 0.4%, respectively.

These observations are not self-consistent because they contradict one another. On one hand, the pole figures reveal significant reorientation of the basal poles suggestive of considerable extension twinning, but the insignificant change in twin volume fraction suggests very little extension twinning. Note that it is possible that some grains have been fully consumed by the $\{10\bar{1}2\}$ extension twins, leaving few twin boundaries to be observed from the EBSD map. One major drawback of shock recovery experiments is the existing knowledge gap between the ambient and end states; to bridge this knowledge gap, we have successfully conducted time-resolved *in situ* synchrotron XRD shock experiments coupled with shock wave profile measurements on FG AMX602 magnesium at the Dynamic Compression Sector (Advanced Photon Source, APS, Argonne National Laboratory, USA). We report on the real time and unequivocal observation of significant texture changes during shock compression and release, indicative of twinning-detwinning. These results have unraveled the complex and contradictory results derived from shock recovery experiments on this textured FG AMX602 magnesium alloy. They have also shed light on the stress release phase in shock-compressed solids, which is not well understood and have plagued the shock compression science community for over six decades.

II. MATERIALS AND METHODS

A. Materials

For this study we used noncombustible FG AMX602 (Mg-6%Al-0.5%Mn-2%Ca, in wt. %) Mg alloy supplied by the Joining and Welding Research Institute, Osaka University, Japan. The AMX602 Mg alloy powder was produced using the spinning water atomization process (SWAP) by combining gas atomization with water atomization, which results in an extremely high solidification rate of approximately 10^6 K/s; producing particle aggregates with irregular shapes ranging in size from 1.0 to 5.0 mm and submicrometer-sized grain structure (1 μm or smaller) [40–42]. The particle aggregates were subsequently consolidated into billets by green compaction at room temperature and hot extruded between 573 and 673 K into rectangular plates having dimensions of 25.4 mm (thickness) by 101.6 mm (width) by 1000.0 mm (length) with an average grain size of 3.41 μm. A more detailed characterization of this Mg alloy is in the open literature [40–42]. Plate impact samples with dimensions of 19.0 mm (diameter) and 1.0 mm (thick) were fabricated using wire electrodischarge
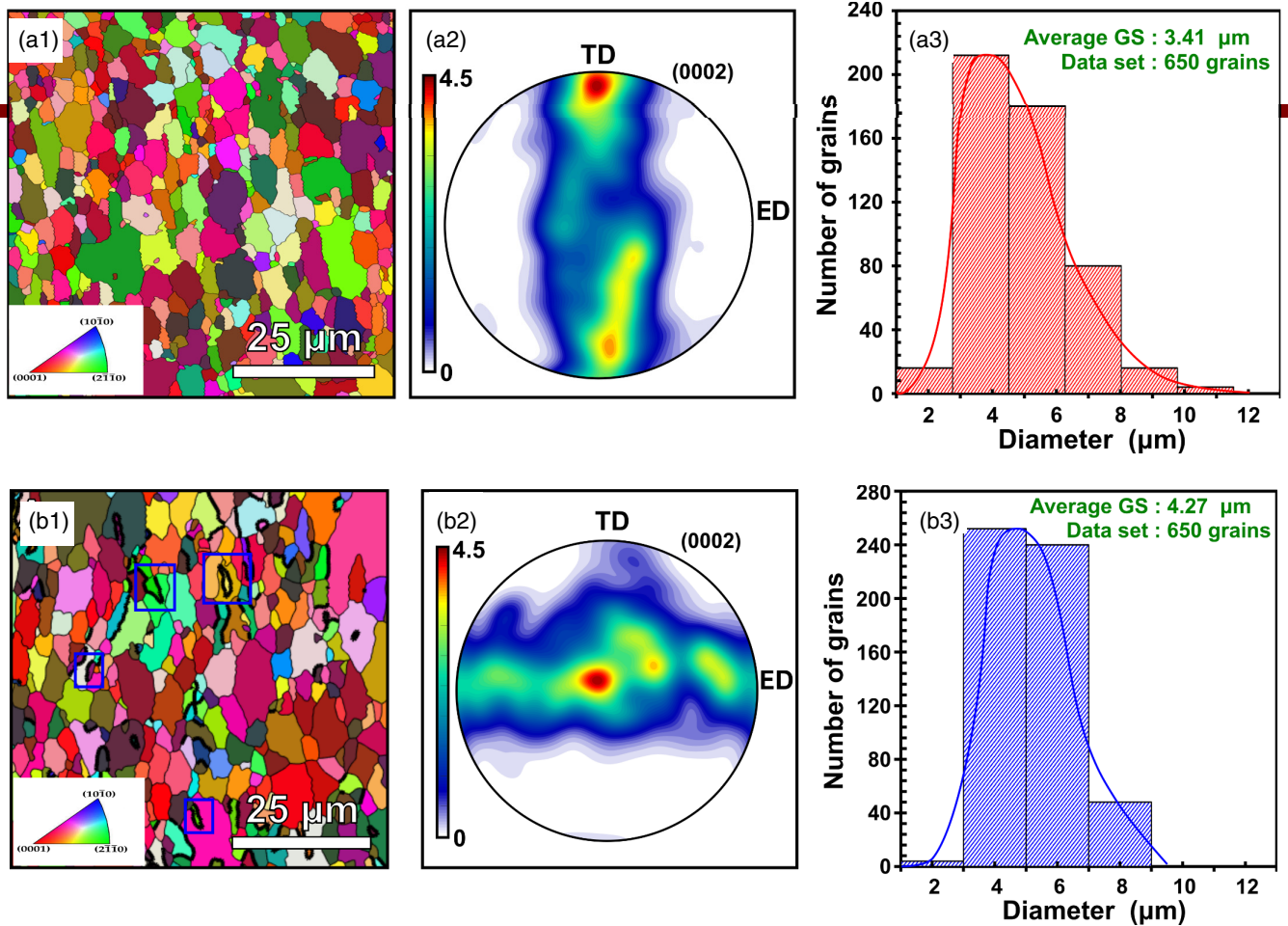
FIG. 1. Grain orientation and size statistics. (a1) The grain orientation map, (a2) basal (0002) pole figure, and (a3) grain size distribution of the as-received (preshock state) AMX602 magnesium. (b1) The grain orientation map, (b2) basal (0002) pole figure, and (b3) grain size distribution of the AMX602 magnesium shock compressed along the plate normal (ND) to approximately 3 GPa, then soft recovered (postshock state). The blue squares in (b1) show some residual extension twins in the soft recovered sample.

machining (EDM) from the normal and extrusion direction of the plate.

B. Loading configuration and diffraction geometry

The loading configuration and diffraction geometry we employed for simultaneous multiframe powder diffraction and wave profile measurements on this FG AMX602 Mg alloy are shown in Figs. 2(a) and 2(b), respectively. As shown in Fig. 2(a), planar shock waves were generated in the Mg samples using polycarbonate (PC) impactors with nominal dimensions of 9 mm thick by 12 mm diameter at velocities ranging from 0.7 to 2.1 km/s, corresponding to peak shock stresses ranging from approximately 2.0 to 7.0 GPa, with a 12.7 mm bore single-stage powder gun. A total of four plate impact experiments were conducted, two each in both the plate normal and extrusion directions. We used velocity interferometry system for any reflector (VISAR) to acquire the free surface velocity histories, from which the steady state Hugoniot stresses were determined. The tilt angles at impact were calculated using the breakout times acquired from three photon Doppler velocimetry (PDV) probes spaced at 120° apart with respect to their locations on the free surface of the

sample. All tilt angles for all experiments were determined to be less than 5 mrad.

All *in situ* XRD measurements were made using an x-ray flux spectrum peaked at 23 keV (0.54 Å wavelength) with a full-width-at-half-maximum bandwidth of about 0.6 keV in single bunch of the APS storage ring operated in 24-bunch mode. For each experiment, four x-ray detectors recorded four images at an interval of 153.4 ns with exposure time of approximately 100 ps. This time interval allows for XRD images to be acquired at the ambient state (frame 1), shock state (frame 2), stress release state (frame 3), and first reverberation from PC/Mg impact interface (frame 4) sequentially. The acquired XRD data were analyzed using FIT2D [43] to study texture evolution and hence, the twinning-detwinning behavior between the various loading and unloading states in this FG AMX602 Mg.

The illustrations in Figs. 2(c) and 2(d) are designed to help interpret the acquired shock wave profile and XRD data. It is evident from Fig. 2(c) that shocking along the plate normal direction results in simultaneous lattice compression along the $\langle c \rangle$-axis, perpendicular to the $\langle c \rangle$ axis, and off-axis compression depending on the grain orientation. While Fig. 2(d) shows that shocking along the plate extrusion
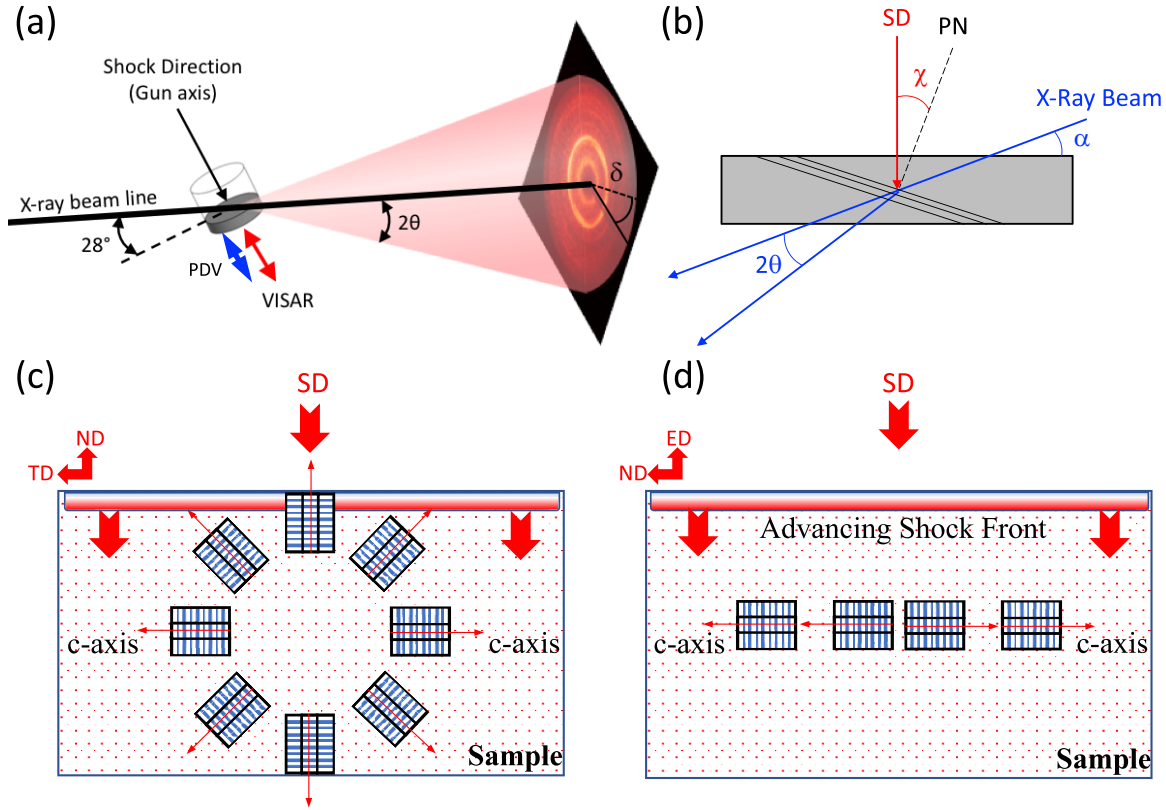
FIG. 2. Experimental loading configuration and diffraction geometry for *in situ*, time-resolved synchrotron powder diffraction and free surface velocity measurements on shock-compressed FG AMX602 magnesium. (a) The x-ray angle of incidence (α) relative to the impact surface was 28° for all transmission experiments and δ is the azimuthal angle. (b) The diffraction geometry shows the relationships between the scattering angle (2θ), shock direction (SD), lattice plane normal (PN), and the angle between the lattice plane normal and shock direction (χ). An illustration of the lattice orientation is shown with respect to the shock loading direction in the (c) plate normal and (d) extrusion directions. ND, TD, and ED represents the normal, transverse, and extrusion directions.

direction implies lattice compression almost perpendicular to the $\langle c \rangle$ axis only. Both loading directions are favorable for activating the $\{10\bar{1}2\}$ extension twinning because they allow for compression perpendicular to the $\langle c \rangle$ axis. However, the loading direction shown in Fig. 2(c) is also favorable for activating the $\{10\bar{1}2\}$ extension twinning on release from the shock state [6]. Therefore, to study texture evolution and the twinning-detwinning behavior of this FG AMX602 Mg, we monitor the diffraction intensity of the basal (0002) reflection, which is the most sensitive indicator for $\{10\bar{1}2\}$ extension twinning.

III. RESULTS AND DISCUSSION

A. Free surface velocity and x-ray diffraction measurements

The resulting free surface velocity histories and corresponding Lagrangian (x-t) diagrams obtained using the Ale3D Hydrocode [44] are shown in Figs. 3(a)–3(d). The figures correspond to impact velocities of 775 (ND), 2034 (ND), 762 (ED), and 2043 m/s (ED), respectively. The resultant peak shock stresses are approximately 2.0, 7.1, 1.9, and 7.1 GPa, respectively. The Lagrangian diagram and corresponding free surface velocity history for the plate normal direction ($\sim$2.0 GPa) shown in Figs. 3(a1) and 3(a2) reveal a two-wave structure. A sharp jump (elastic shock) is first observed up

to the Hugoniot elastic limit (HEL), which is immediately followed by a sharp plastic rise (shock wave). Note that the impact interface on all the Lagrangian diagrams is located at $x = 0$ and only 0.5 mm of the 9.0 mm long PC impactor is revealed in the figure for clarity. The elastic shock arrives at the free surface at $\sim$0.24 μs after impact, then the stress release phase immediately begins and ends at $\sim$0.42 μs after impact. The steady-state free surface velocity starts at point 1 and ends at point 2. The first reverberation from the PC/Mg impact interface reaches the Mg free surface at $\sim$0.50 μs after impact. Similar observations were made in Figs. 3(b), 3(c), and 3(d). The dashed lines shown in the figures represent the times at which the XRD frames were acquired relative to impact. It is evident from the Lagrangian diagrams shown in Figs. 3(a1), 3(b1), 3(c1), and 3(d1) that the first XRD frames (1) were acquired when the FG AMX602 Mg was less than 50% shocked. Therefore, the integrated diffraction data reported in this paper did not include frame 1, the ambient conditions reported were acquired under static conditions prior to the shock XRD experiments. Also, from Fig. 3(a1) it was estimated that the Mg sample was $\sim$80% shocked at frame 2 and $\sim$87% released at frame 3. Similarly, from Figs. 3(b1), 3(c1), and 3(d1), it was estimated that the material was fully shocked and $\sim$75% released, $\sim$88% shocked and $\sim$80% released, and $\sim$90% shocked and $\sim$70% released,
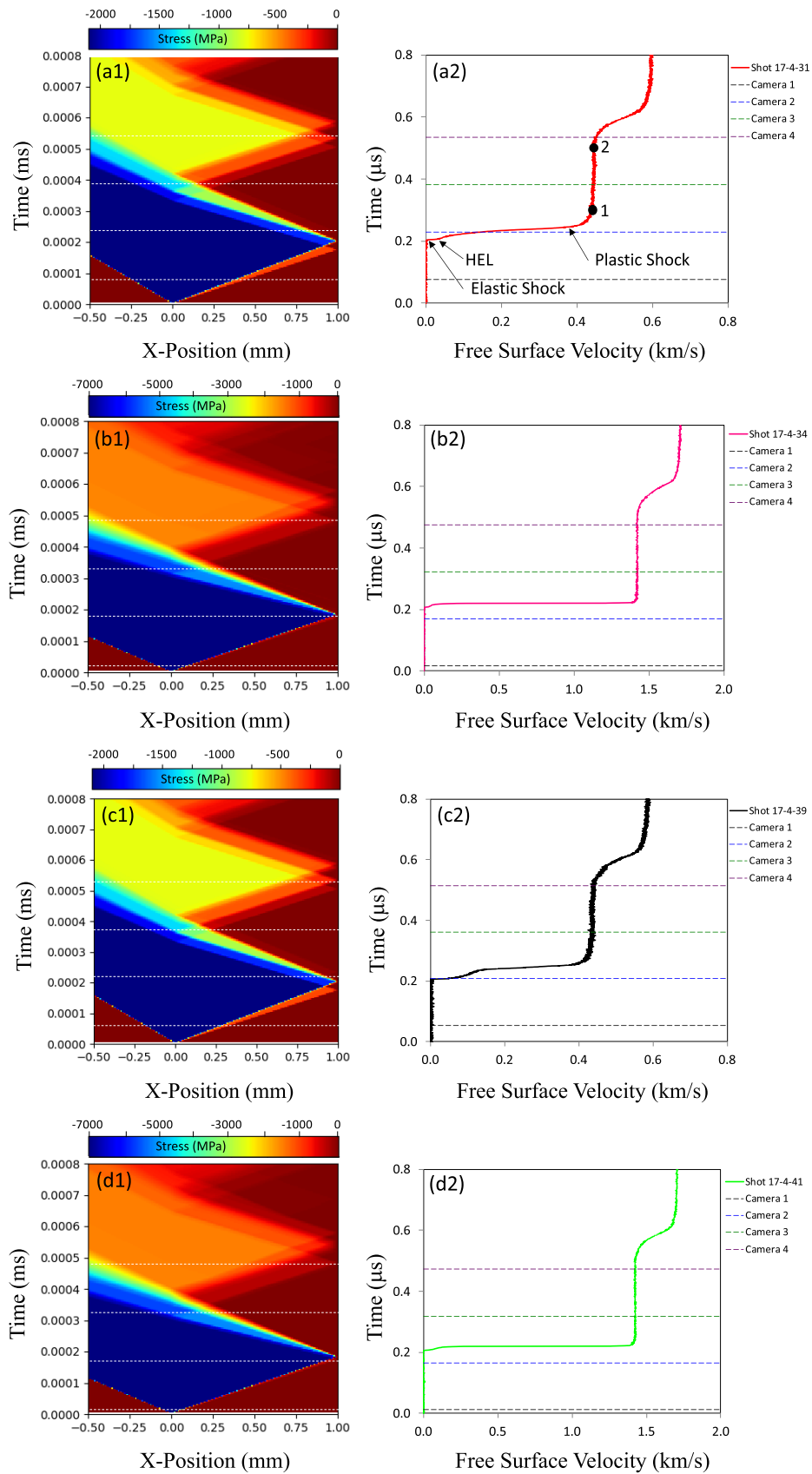
FIG. 3. Position-time (Lagrangian) diagrams and VISAR velocity profiles of shock-compressed FG AMX602 magnesium (a) ND at ~2.0 GPa, (b) ND at ~7.1 GPa, (c) ED at ~1.9 GPa, and (d) ED at ~7.1 GPa. The dashed lines correspond to all four XRD frames relative to impact and are separated by 153.4 ns.

TABLE I. *In situ* XRD experimental parameters.

	Shot 17-4-031	Shot 17-4-034	Shot 17-4-039	Shot 17-4-041
Impactor velocity (m/s)	775	2034	762	2043
Shock stress (GPa)	2.0	7.1	1.9	7.1
XRD frame 1 times relative to impact (ns)	75	16	54	12
XRD frame 2 times relative to impact (ns)	229	169	208	166
XRD frame 3 times relative to impact (ns)	382	323	361	319
XRD frame 4 times relative to impact (ns)	536	476	515	472
Ambient sample to detector distance (mm)	144.7	144.7	144.6	144.7
Frame 1 sample to detector distance for XRD (mm)	142.0	142.2	141.9	142.3
Frame 2 sample to detector distance for XRD (mm)	141.8	141.7	141.7	141.8
Frame 3 sample to detector distance for XRD (mm)	141.7	141.2	141.6	141.3
Frame 4 sample to detector distance for XRD (mm)	141.4	140.6	141.4	140.7

respectively, at frames 2 and 3. Pertinent information for all XRD shock experiments are listed in Table I.

The integrated diffraction profiles acquired from the plate normal and extrusion directions are shown in Fig. 4. The figures show the evolution of the integrated diffraction profiles between the ambient, shock, release, and first reverberation states. Figure 4(a) reveals that the first order pyramidal $(10\bar{1}1)$, basal (0002), and prismatic $(01\bar{1}0)$ planes exhibited the strongest diffraction intensities at the ambient state. When

this FG AMX602 Mg is shock compressed, the XRD signature of the amorphous PC impactor is revealed at $2\theta \approx 6°$. The figure also shows significant losses in peak intensity and likewise, significant peak shift towards the higher 2θ values were observed at the higher shock stresses. Since the lattice spacing d is inversely proportional to the Bragg angle, this suggests lattice compression. However, when this FG AMX602 Mg is released from the shock state, we observe gains in peak intensity at the stress release and first reverberation states.
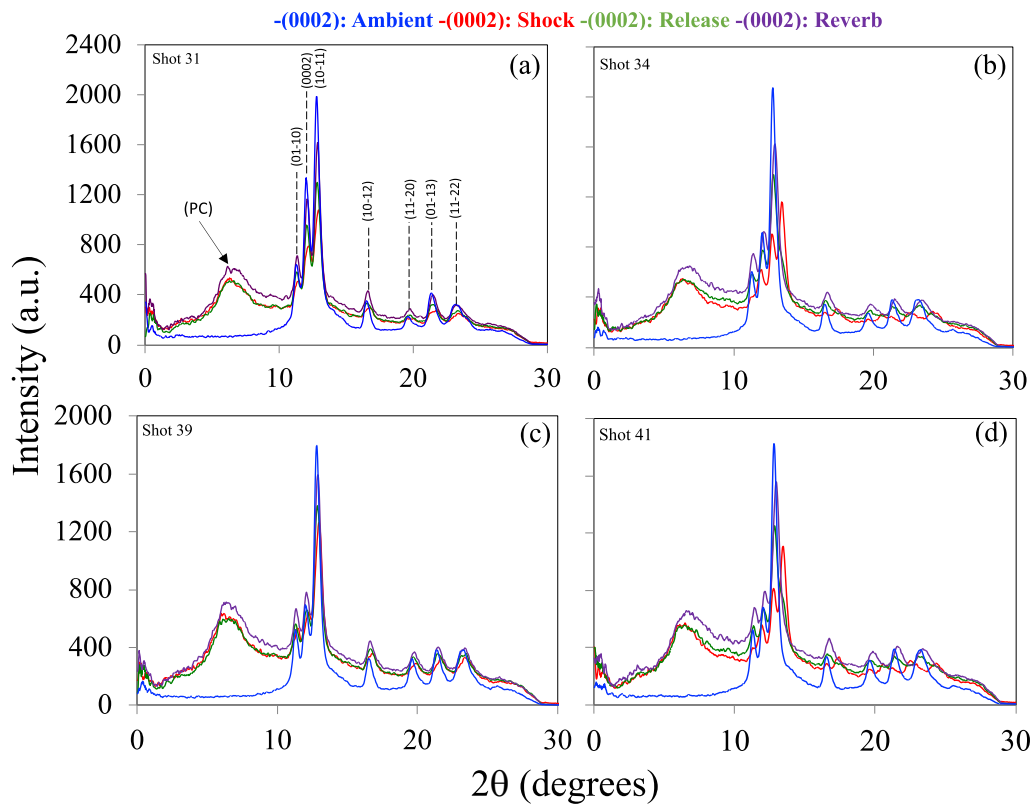

FIG. 4. Synchrotron x-ray diffraction patterns of FG AMX602 magnesium (a) at the ambient (cyan), shock (∼2.0 GPa red), release (green), and first reverberation (magenta) states along the plate normal direction (b) at the ambient, shock (∼7.1 GPa), release, and first reverberation states along the plate normal direction. Similarly, (c) and (d) represent the diffraction patterns at the ambient, shock, release, and first reverberation states for peak shock stresses of ∼1.9 and ∼7.1 GPa, respectively, along the plate extrusion direction. Diffraction intensities from various lattice planes and the amorphous polycarbonate (PC) impactor are identified in (a).
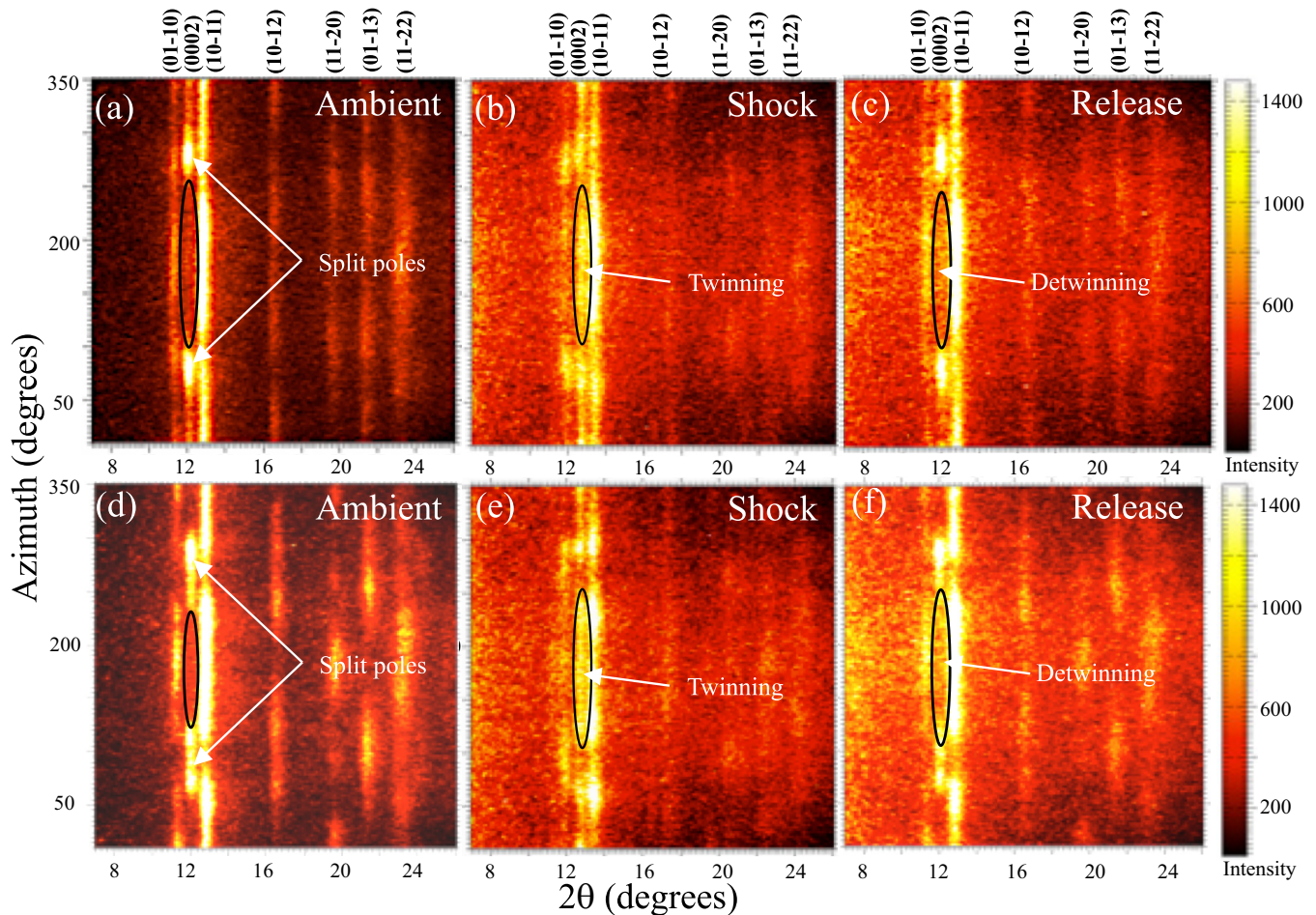
FIG. 5. Diffraction powder ring intensities plotted as azimuth versus 2θ for FG AMX602 Mg (a) ambient, (b) shock ($\sim$7.1 GPa), and (c) release states along the plate normal direction, shot 34. Similarly, (d) represents the ambient, (e) shock ($\sim$7.1 GPa), and (f) release states along the plate extrusion direction, shot 41. The powder rings are discontinuous indicating a textured material. The 2θ ambient positions for the three high reflections, prismatic $(01\bar{1}0)$, basal (0002), and first order pyramidal $(10\bar{1}1)$ diffraction peaks in (a) and (d) are 11.27°, 12.01°, and 12.80°, respectively.

Also, the peaks revert approximately to their original 2θ positions, which suggests that the lattices are approximately free of stress. These observations are consistent for all peak shock stresses and loading directions studied [see Figs. 4(a)–4(d)].

B. Real-time observation of twinning and detwinning

Figure 5 presents the Debye diffraction powder ring intensities between 10° and 350° (to avoid the x-ray beam stop) for all crystal lattice planes, plotted as a function of the azimuthal angle (δ) and scattering angle (2θ). Figures 5(a)–5(c) represent the ambient, shock ($\sim$7.1 GPa), and release states, respectively, in the plate normal direction. While Figs. 5(d)–5(f) represent the ambient, shock ($\sim$7.1 GPa), and release states, respectively, in the plate extrusion direction. The results show that the diffraction intensity of the basal (0002) plane, with a discontinuous powder diffraction ring between the split poles highlighted by the ellipse at the ambient state, becomes continuous at the shock state as the powder diffraction ring develops a strong intensity between the two poles, as shown by data enclosed by the ellipse in Fig. 5(b). However, when the material is released from the shock state, the continuous

intensity reverts back to a strong basal (0002) texture as evident in Fig. 5(c). Similar observations were made for the extrusion direction. The diffraction intensity of the basal (0002) plane with a discontinuous powder diffraction ring [Fig. 5(d)] becomes continuous at the shock state [see Fig. 5(e)] and then reverts back to the strong basal (0002) texture [see Fig. 5(f)]. These observations strongly suggest twinning during shock compression and detwinning during stress release, in both normal and extrusion directions in this FG AMX602 Mg. We omit the first reverberation states in both directions for clarity but they reveal strong basal (0002) texture.

C. Texture evolution

To further examine the evolution of texture as a function of loading history, the Debye diffraction powder rings were segmented into arcs of 5° and integrated with FIT2D from 10° to 350° about the azimuthal angle δ. This produces 70 segments from which the diffraction intensity was plotted as a function of tilt angle χ ranging from 0° to 180° as shown in Fig. 6. For the transmission diffraction geometry shown in Fig. 2(b), the angle of incidence of the synchrotron
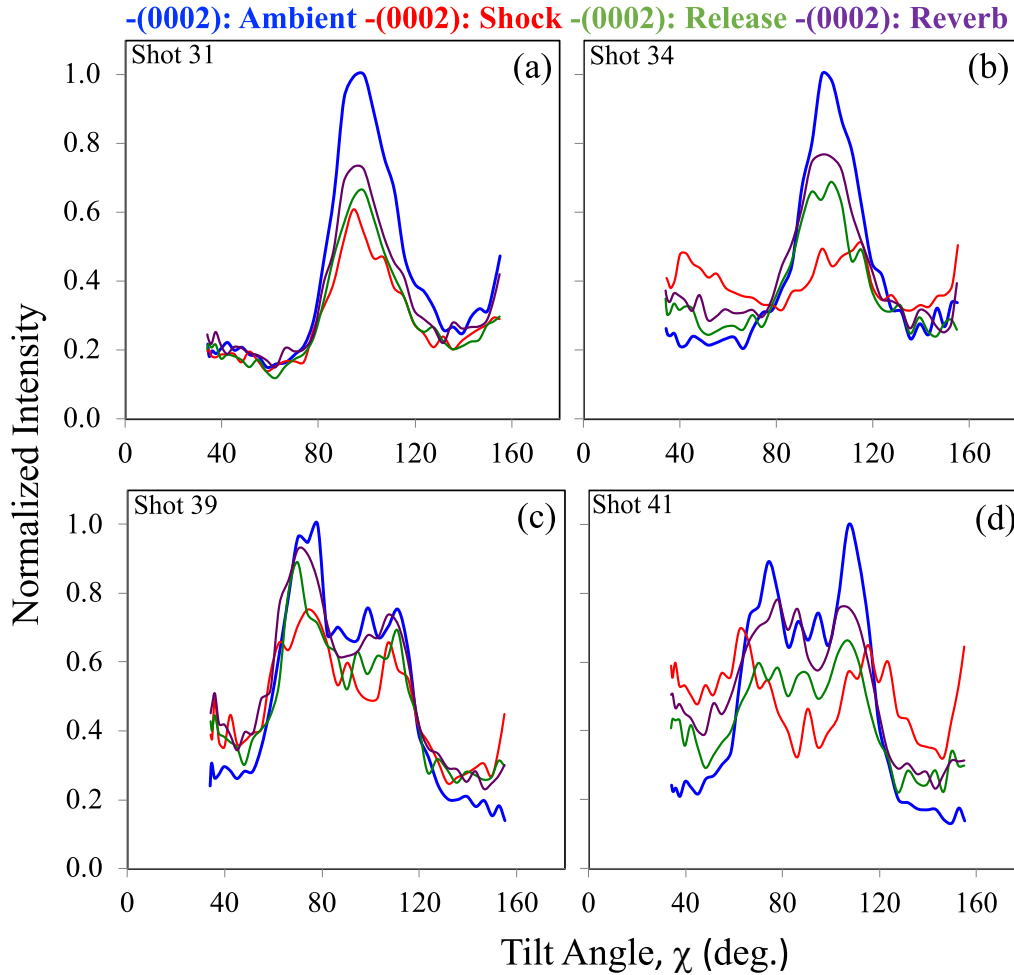
FIG. 6. Normalized intensity of diffraction as a function of tilt angle χ for basal (0002) planes in FG AMX602 magnesium shock compressed to (a) ~2.0 GPa and (b) ~7.1 GPa, respectively, along the plate normal direction. Similarly, (c) and (d) represents the intensity of diffraction as a function of tilt angle χ for basal (0002) planes shock compressed to ~1.9 and ~7.1 GPa, respectively, along the plate extrusion direction.

x-ray beam relative to the impact surface is α. The angle between the shock loading or gun axis and the diffracting plane normal χ_{hkl} was then calculated for this loading and diffraction geometry using the following equation [45,46]:

$$\cos \chi_{hkl} = -\cos \alpha \cos \delta \cos \theta_{hkl} - \sin \alpha \sin \theta_{hkl}, \quad (1)$$

where $\alpha = 28°$, θ is the Bragg angle, and δ is the azimuthal angle in the plane of the detector. We clearly observed from Fig. 6 intensity variations as a function of χ (texture evolution) in both the normal and extrusion directions. Referencing Fig. 2(b), the diffraction intensity for a single crystal magnesium would register zero at $\chi = 62°$ (when the basal plane is perpendicular to the x-ray beam) and $\chi = 152°$ (when the basal plane is parallel to the incident x-ray beam), respectively; Bragg condition is not satisfied in either orientation. However, for this textured FG AMX602 Mg alloy, the diffraction intensity does not register zero at the same χ positions because the poles have an estimated spread of approximately $\pm 30°$ about the transverse direction as evident in Fig. 1(a2). This implies that some of the basal planes are oriented such that Bragg condition is satisfied and others are oriented such that Bragg condition is not satisfied.

During $\{10\bar{1}2\}$ extension twinning, the twinned grain is reoriented such that the $\langle c \rangle$ axis rotates by approximately $\pm 90°$ relative to the parent grain. This reorientation causes intensity interchange between the parent and twin reflection pair (0002) and $(10\bar{1}0)$ [47–50]. Therefore, an intensity reduction in (0002) reflection triggers an intensity increase in $(10\bar{1}0)$ reflection and vice versa. We observe from Figs. 6(a) and 6(b) significant reductions in intensity for the (0002) reflection between $80° < \chi < 130°$ when this FG AMX602 Mg is shock compressed to ~2.0 and ~7.1 GPa, respectively, along the normal direction. At the stress release state, the diffraction intensity increases in this χ band, then followed by a further increase at the first reverberation state. The corresponding intensity interchanges for the same χ range are shown in Figs. 7(a) and 7(b), respectively. It is evident from the figures that a reduction in intensity for the basal (0002) reflection between $80° < \chi < 130°$ triggers an increase in prismatic $(10\bar{1}0)$ reflection when this FG AMX602 Mg is shock compressed along the normal direction to ~2.0 and ~7.1 GPa, respectively. Similar observations were made for the extrusion direction. We observe from Figs. 6(c) and 6(d) significant reductions in intensity for the (0002) reflection for
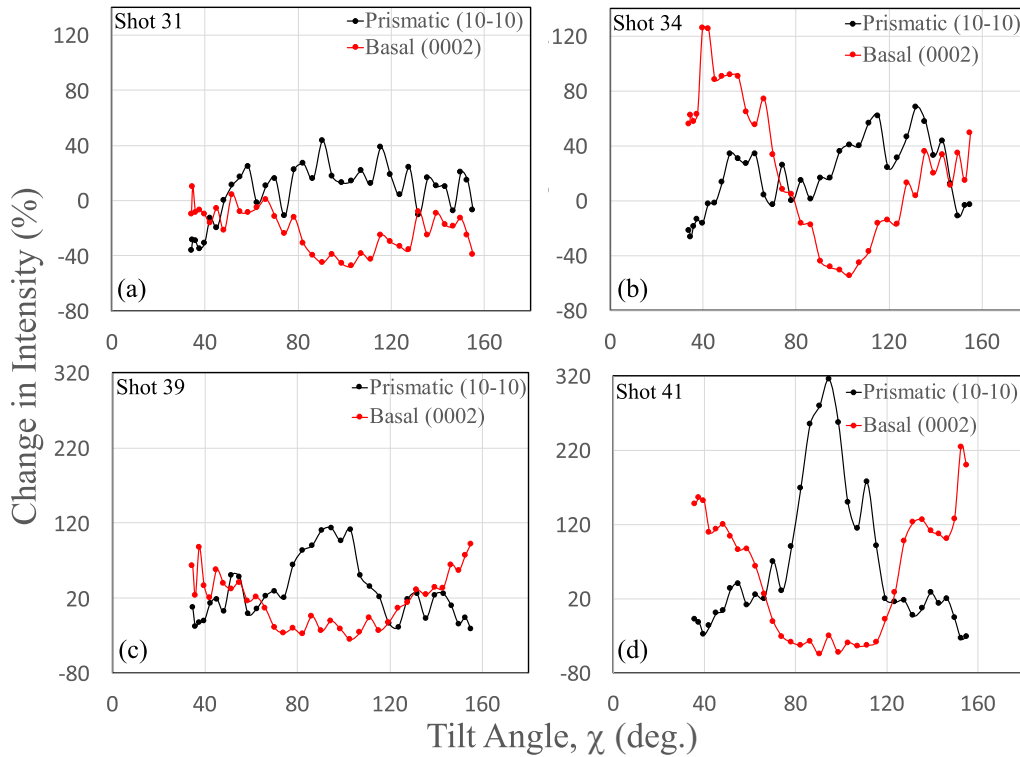
FIG. 7. Intensity interchange between the basal (0002) and prismatic ($10\bar{1}0$) planes in FG AMX602 magnesium shock compressed to (a) ~ 2.0 GPa and (b) ~ 7.1 GPa, respectively, along the plate normal direction. Similarly, (c) and (d) represents the intensity interchange between the basal (0002) and prismatic ($10\bar{1}0$) planes shock compressed to ~ 1.9 and ~ 7.1 GPa, respectively, along the plate extrusion direction.

shock stresses at ~ 1.9 and ~ 7.1 GPa, respectively. However, for the extrusion direction, the intensity interchanges occur between $60° < \chi < 120°$. The intensity interchanges for the extrusion direction are shown in Figs. 7(c) and 7(d) and they clearly reveal that when the intensity of the basal (0002) reflection decreases, it triggers an increase in intensity for the prismatic ($10\bar{1}0$) reflection. These results in entirety affirm that twinning-detwinning occurs between $80° < \chi < 130°$ for the normal direction and between $60° < \chi < 120°$ for the extrusion direction.

D. Bridging the existing knowledge gap

Extruded magnesium and its alloys when compressed parallel to the extrusion direction (C//ED) beyond their elastic limit and in this case, the Hugoniot elastic limit, can form large volumes of $\{10\bar{1}2\}$ extension twins. Only the $\{10\bar{1}2\}$ extension twinning (dominant mode) and low-CRSS $\langle a \rangle$ basal slip deformation mechanisms are required to accommodate plastic deformation when compressed along the extrusion direction (C//ED), while all other deformation mechanisms play a lesser role [51–54]. From Fig. 2(d), shocking along the plate extrusion direction implies lattice compression almost perpendicular to the $\langle c \rangle$ axis only and this orientation is well suited for activating the $\{10\bar{1}2\}$ extension twins. There are six possible crystallographically equivalent $\{10\bar{1}2\}$ twin variants in magnesium: $(10\bar{1}2)[\bar{1}011]$, $(01\bar{1}2)[0\bar{1}11]$, $(\bar{1}012)[10\bar{1}1]$, $(\bar{1}102)[1\bar{1}01]$, $(0\bar{1}12)[01\bar{1}1]$, and $(01\bar{1}2)[0\bar{1}11]$, and the twinning Schmid factor (SF) plays an important role on which twin variants are activated under stress [16]. As the tilt angle

deviates from the ideal case, i.e., loading direction parallel to the $\langle a \rangle$ axis or $\langle c \rangle$ axis, the SF decreases [16]. The twin variants with the highest SF value are likely to be actived and dominate the twinning behavior of this FG Mg alloy. From the illustrations shown in Figs. 8(a) and 8(b), when this extruded FG AMX602 Mg is compressed along the plate extrusion direction to the stable shock state, the $\langle c \rangle$ axis are reoriented by approximately 90° and are symmetrically distributed about the ED; this is typical of $\{10\bar{1}2\}$ extension twinning dominated texture evolution in extruded Mg [51–54]. However, owing to the symmetrical distribution of the $\langle c \rangle$ axes about the ED, the SF of all six twin variants are approximately equal. Hence, during stress release (tensile stresses along the ED) all six twin variants can be equally active and the $\langle c \rangle$ axes are reoriented back to their original position by detwinning as illustrated in Fig. 8 from two views, the ND-TD and ED-TD planes. This is consistent with the observations made by Culbertson *et al.* [53] for extruded pure polycrystalline Mg rod, which were precompressed and subsequently pulled in tension.

On the contrary, when this extruded FG AMX602 Mg is shock compressed along the plate normal direction (C⊥ED) as illustrated in Fig. 2(c), this results in simultaneous lattice compression along the $\langle c \rangle$ axis, perpendicular to the $\langle c \rangle$ axis, and off-axis compression depending on the grain orientation. Although this loading configuration has limited lattice orientations favorable for $\{10\bar{1}2\}$ extension twinning, only the low-CRSS $\langle a \rangle$ basal slip (dominant mode) and $10\bar{1}2$ extension twinning deformation mechanisms are required to accommodate plastic deformation, while all other deformation mechanisms play a lesser role [51]. As the illustrations
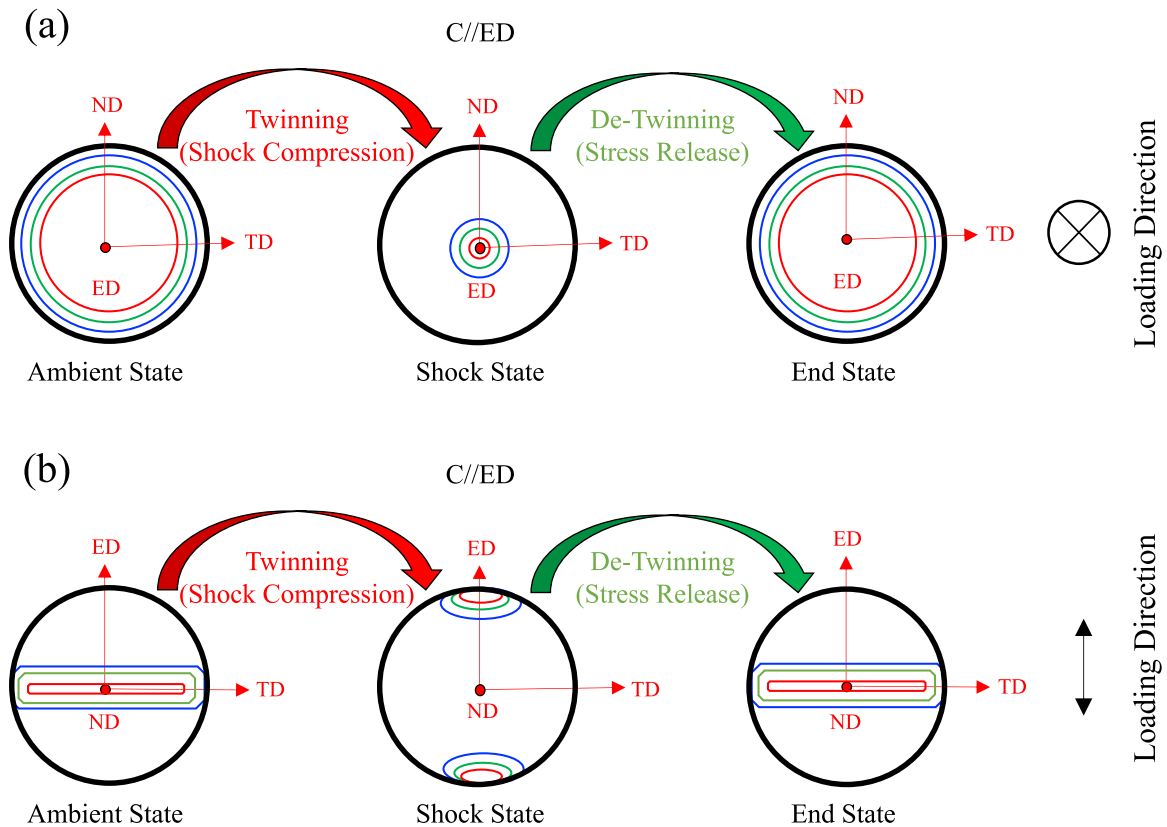
FIG. 8. Illustrations of texture evolution of the basal (0002) poles in FG AMX602 magnesium samples during shock compression and stress release along the plate extrusion direction (C//ED). (a) ND-TD plane view and (b) ED-TD plane view.

in Figs. 9(a) and 9(b) show, as this extruded FG AMX602 Mg is compressed along the plate normal direction to the stable shock state, the basal poles are reoriented by approximately 90° about the ED towards the ND, typical of {10$\bar{1}$2} extension twinning dominated texture evolution in extruded Mg [51–54]. However, for this case, the ⟨c⟩ axes are not symmetrically distributed about the ND. Instead, there is a large ⟨c⟩-axis orientation spread along the TD (elliptical in shape). Similar observations were made at lower strain rate experiments for strains up to 10% [51,52]. This implies that the tilt angle deviation from the ideal case is larger in the TD as illustrated in Fig. 9(a) compared to the spread in the ED. The SF of the twin variants, which are aligned with the ED, are expected to be larger than those aligned with the TD. During stress release (tensile stresses along the ND) the twin variants aligned with the ED are expected to be activated because they possess the highest SF. For this case, the ⟨c⟩ axes are reoriented randomly about the TD due to detwinning as illustrated in Figs. 9(a) and 9(b) not the ED as in the previous case. In addition, a possible reason why the measured twin volume fraction after shock compression and release is low but the intensity in the pole figure is quite strong for the shock recovered sample is that detwinning during unloading may be incomplete. Twinning in FG Mg samples is quite different from twinning in coarse grained Mg samples. During twinning in FG Mg samples, some grains can be entirely twinned without leaving observable twin boundaries within the grains. Detwinning becomes difficult

due to the lack of twin boundaries and the process may be hindered.

IV. SUMMARY AND CONCLUSIONS

FG AMX602 magnesium alloy shock compressed along the plate normal to approximately 3 GPa and then soft recovered, shows that the majority of the basal poles were reoriented about the plate normal by approximately 90° suggestive of significant {10$\bar{1}$2} extension twinning. However, this observation was contradicted by the fact that the twin volume fraction of the as-received and shock recovered samples were approximately 0% and 0.4%, respectively, suggestive of insignificant {10$\bar{1}$2} extension twinning. These observations are not consistent and were elucidated using time-resolved *in situ* synchrotron x-ray diffraction shock experiments. Significant twinning during shock compression and detwinning during stress release were observed real time in this FG AMX602 magnesium alloy via texture evolution studies. These twinning-detwinning observations were validated through the intensity interchange between the parent and twin reflection pair (0002)-basal and (10$\bar{1}$0)-prismatic, which normally occur during {10$\bar{1}$2} extension twinning in materials with hexagonal closed pack lattice structure. We conclude that these observations show that detwinning is responsible for the insignificant change in twin volume fraction between the ambient and shock recovered samples but acknowledging that some grains may have been entirely twinned without leaving
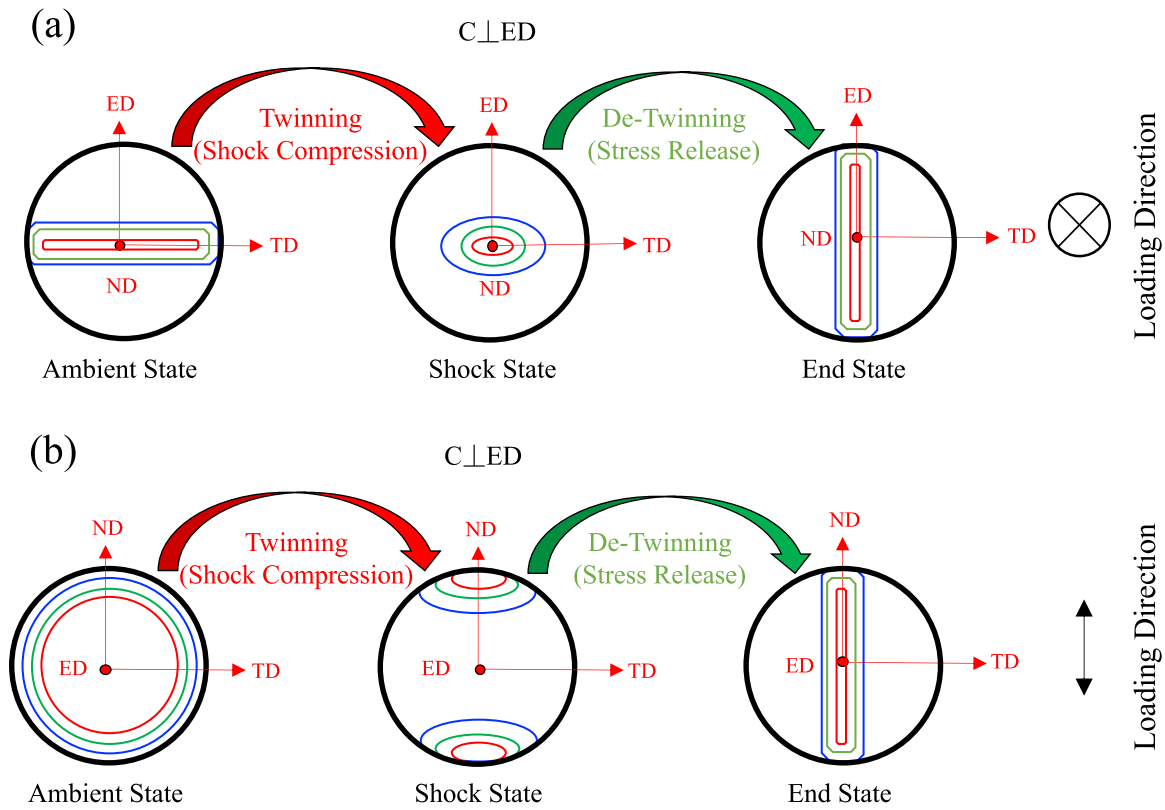
FIG. 9. Illustrations of texture evolution of the basal (0002) poles in FG AMX602 magnesium samples during shock compression and stress release along the plate normal direction (C⊥ED). (a) ED-TD plane view and (b) ND-TD plane view.

observable twin boundaries within the grains. It is also postulated that the high Schmid factor of the twin variants, which are aligned with the ED, is responsible for the 90° reorientation of the basal poles about the ND observed for the shock recovered samples. Time-resolved *in situ* synchrotron x-ray diffraction shock experiments provide a fundamental understanding of the complex twinning-detwinning behavior of this textured FG AMX602 magnesium alloy and helped to bridge the existing knowledge gap in shock recovery experiments.

[1] C. S. Smith, Metallographic studies of metals after explosive shock, Trans. Met. Soc. AIME **212**, 574 (1958).

[2] F. Zhang, M. Hao, F. C. Wang, C. W. Tan, X. D. Yu, H. L. Ma, and H. N. Cai, Role of (10$\bar{1}$2) twinning and detwinning in the shock-hardening behavior of rolled Mg–3Al–1Zn alloy, Scr. Mater. **67**, 951 (2012).

[3] G. I. Kanel, G. V. Garkushin, A. S. Savinykh, S. V. Razorenov, T. De Resseguier, W. G. Proud, and M. R. Tyutin, Shock response of magnesium single crystals at normal and elevated temperatures, J. Appl. Phys. **116**, 143504 (2014).

[4] L. Farbaniec, C. L. Williams, L. Kecskes, K. T. Ramesh, and R. Becker, Microstructural effects on the spall properties of ecae-processed AZ31b magnesium alloy, Int. J. Impact Eng. **98**, 34 (2016).

[5] L. Farbaniec, C. L. Williams, L. Kecskes, R. Becker, and K. T. Ramesh, Spall response and failure mechanisms associated with a hot-extruded AMX602 Mg alloy, Mater. Sci. Eng. A **707**, 725 (2017).

[6] S. J. Turneaure, P. Renganathan, J. M. Winey, and Y. M. Gupta, Twinning and Dislocation Evolution During Shock Compression and Release of Single Crystals: Real-Time X-ray Diffraction, Phys. Rev. Lett. **120**, 265503 (2018).

[7] C. E. Wehrenberg, D. McGonegle, C. Bolme, A. Higginbotham, A. Lazicki, H. J. Lee, B. Nagler, H. S. Park, B. A. Remington,

R. E. Rudd, M. Sliwa, M. Suggit, D. Swift, F. Tavella, L. Zepeda-Ruiz, and J. S. Wark, In situ x-ray diffraction measurement of shock-wave-driven twinning and lattice dynamics, Nature (London) **550**, 496 (2017).

[8] M. Sliwa, D. McGonegle, C. Wehrenberg, C. A. Bolme, P. G. Heighway, A. Higginbotham, A. Lazicki, H. J. Lee, B. Nagler, H. S. Park, R. E. Rudd, M. J. Suggit, D. Swift, F. Tavella, L. Zepeda-Ruiz, B. A. Remington, and J. S. Wark, Femtosecond X-ray Diffraction Studies of the Reversal of the Microstructural Effects of Plastic Deformation During Shock Release of Tantalum, Phys. Rev. Lett. **120**, 265502 (2018).

[9] S. J. Tracy, S. J. Turneaure, and T. S. Duffy, *In Situ* X-ray Diffraction of Shock-Compressed Fused Silica, Phys. Rev. Lett. **120**, 135702 (2018).

[10] E. W. Kelley and W. F. Hosford, Plane-strain compression of magnesium and magnesium alloy crystals, Trans Met Soc AIME **242**, 5 (1968).

[11] M. H. Yoo, Slip twinning and fracture in hexagonal close-packed metals, Metal. Trans. A **12**, 409 (1981).

[12] B. Li and E. Ma, Pyramidal slip in magnesium: Dislocations and stacking fault on the {1011} plane, Philos. Mag. **89**, 1223 (2009).

[13] N. Dixit, K. Y. Xie, K. J. Hemker, and K. T. Ramesh, Microstructural evolution of pure magnesium under high strain rate loading, Acta Mater. **87**, 56 (2015).

[14] V. Kannan, K. Hazeli, and K. T. Ramesh, The mechanics of dynamic twinning in single crystal magnesium, J. Mech. Phys. Solids **120**, 154 (2018).

[15] S. R. Agnew and O. Duygulu, Plastic anisotropy and the role of non-basal slip in magnesium alloy AZ31B, Int. J. Plast. **21**, 1161 (2005).

[16] S. G. Hong, S. H. Park, and C. S. Lee, Role of {10–12} twinning characteristics in the deformation behavior of a polycrystalline magnesium alloy, Acta Mater. **58**, 5873 (2010).

[17] C. Kale, M. Rajagopalan, S. Turnage, B. Hornbuckle, K. Darling, S. N. Mathaudhu, and K. N. Solanki, On the roles of stress-triaxiality and strain-rate on the deformation behavior of AZ31 magnesium alloys, Mater. Res. Lett. **6**, 152 (2018).

[18] H. Yoshinaga and R. Horiuchi, Deformation mechanisms in magnesium single crystals compressed in the direction parallel to hexagonal axis, Trans. Jpn. Inst. Metals **4**, 1 (1963).

[19] J. F. Stohr and J. P. Poirier, Electron-microscope study of pyramidal slip {1122}{1123} in magnesium, Philos. Mag. **25**, 1313 (1972).

[20] T. Obara, H. Yoshinga, and S. Morozumi, {1122}{1123} slip system in magnesium, Acta Metal. **21**, 8451973.

[21] M. H. Yoo, J. R. Morris, K. M. Ho, and S. R. Agnew, Non-basal deformation modes of hcp metals and alloys: Role of dislocation source and mobility, Metal. Mater. Trans. A **33**, 813 (2002).

[22] M. H. Yoo, S. R. Agnew, J. R. Morris, and K. M. Ho, Non-basal slip systems in hcp metals and alloys: Source mechanisms, Mater. Sci. Eng. A **319-321**, 87 (2001).

[23] J. Koike, T. Kobayashi, T. Mukai, H. Watanabe, M. Suzuki, K. Maruyama, and K. Higashi, The activity of non-basal slip systems and dynamic recovery at room temperature in fine-grained AZ31B magnesium alloys, Acta Mater. **51**, 2055 (2003).

[24] C. S. Meredith, J. T. Lloyd, and T. Sano, The quasi-static and dynamic response of fine-grained Mg alloy AMX602: An experimental and computational study, Mater. Sci. Eng. A **673**, 73 (2016).

[25] C. S. Roberts, *Magnesium and Its Alloys* (Wiley, New York, 1960).

[26] R. E. Reed-Hill and W. D. Robertson, Deformation of magnesium single crystals by non-basal slip, JOM **9**, 496 (1957).

[27] S. R. Agnew, M. H. Yoo, and C. N. Tome, Application of texture simulation to understanding mechanical behavior of Mg and solid solution alloys containing Li or Y, Acta Mater. **49**, 4277 (2001).

[28] S. Kleiner and P. J. Uggowitzer, Mechanical anisotropy of extruded Mg–6% Al–1% Zn alloy, Mater. Sci. Eng. A, **379**, 258 (2004).

[29] M. D. Nave and M. R. Barnett, Microstructures and textures of pure magnesium deformed in plane-strain compression, Scr. Mater. **51**, 881 (2004).

[30] A. Serra and D. J. Bacon, A new model for {1012} twin growth in hcp metals, Philos. Mag. A **73**, 333 (1996).

[31] L. Kucherov and E. B. Tadmor, Twin nucleation mechanisms at a crack tip in an hcp material: Molecular simulation, Acta Mater. **55**, 2065 (2007).

[32] A. Serra, D. J. Bacon, and R. C. Pond, The crystallography and core structure of twinning dislocations in hcp metals, Acta Metal. **36**, 3183 (1988).

[33] A. Serra, R. C. Pond, and D. J. Bacon, Computer simulation of the structure and mobility of twinning dislocations in hcp metals, Acta Metal. Mater. **39**, 1469 (1991).

[34] B. Li, S. P. Joshi, O. Almagri, Q. Ma, K. T. Ramesh, and T. Mukai, Rate-dependent hardening due to twinning in an ultra-fine-grained magnesium alloy, Acta Mater. **60**, 1818 (2012).

[35] P. Renganathan, J. M. Winey, and Y. M. Gupta, Shock compression and release of a-axis magnesium single crystals: Anisotropy and time dependent inelastic response, J. Appl. Phys. **121**, 035901 (2017).

[36] H. Yoshinaga, T. Obara, and S. Morozumi, Twinning deformation in magnesium compressed along the c-axis, Mater. Sci. Eng. **12**, 255 (1973).

[37] Q. Yang and A. K. Ghosh, Deformation behavior of ultrafine-grain (UFG) AZ31B Mg alloy at room temperature, Acta Mater. **54**, 5159 (2006).

[38] B. Li, S. Joshi, K. Azevedo, E. Ma, K. T. Ramesh, R. B. Figueiredo, and T. G. Langdon, Dynamic testing at high strain rates of an ultrafine-grained magnesium alloy processed by ECAP, Mater. Sci. Eng. **517**, 24 (2009).

[39] S. R. Kada, Deformation of magnesium alloys during laboratory scale in-situ x-ray diffraction, Technical report, Deakin University, 2013.

[40] K. Kondoh, E.-S. A. Hamada, H. Imai, J. Umeda, and T. Jones, Microstructures and mechanical responses of powder metallurgy non-combustive magnesium extruded alloy by rapid solidification process in mass production, Mater. Design **31**, 1540 (2010).

[41] E. Ayman, J. Umeda, and K. Kondoh, Application of rapid solidification powder metallurgy to the fabrication of high-strength, high-ductility Mg–Al–Zn–Ca–La alloy through hot extrusion, Acta Mater. **59**, 273 (2011).

[42] J. Liao, M. Hotta, and Y. Mori, Improved corrosion resistance of a high-strength Mg–Al–Mn–Ca magnesium alloy made by rapid solidification powder metallurgy, Mater. Sci. Eng. A **544**, 10 (2012).

[43] A. P. Hammersley, Fit2d: An introduction and overview, European Synchrotron Radiation Facility Internal Report ESRF97HA02T, 68:58, 1997.

[44] C. R. Nobel, A. T. Anderson, N. R. Barton, J. A. Bramwell, and A. Capps *et al..*, ALE3D: An arbitrary Lagrange/Eulerian multi-physics code., Lawrence Livermore National Laboratory report, Livermore, CA. LLNL-TR-732040, 2017.

[45] S. Turneaure (unpublished, 2019).

[46] C. L. Williams (private communication, 2019).

[47] M. A. Gharghouri, G. C. Weatherly, J. D. Embury, and J. Root, Study of the mechanical properties of Mg-7.7 at.% Al by in-situ neutron diffraction, Philos. Mag. A **79**, 1671 (1999).

[48] D. W. Brown, S. R. Agnew, M. A. M. Bourke, T. M. Holden, S. C. Vogel, and C. N. Tomé, Internal strain and texture evolution during deformation twinning in magnesium, Mater. Sci. Eng. A **399**, 1 (2005).

[49] O. Mura´nsky, D. G. Carr, S. P. Sˇittner, and E. C. Oliver, *In situ* neutron diffraction investigation of deformation twin-

ning and pseudoelastic-like behaviour of extruded AZ31 magnesium alloy, Int. J. Plast. **25**, 1107 (2009).

[50] Z. Wang, P. A. Lynch, S. R. Kada, N. Armstrong, E. B. Motlagh, J. A. Kimpton, and M. R. Barnett, A high-resolution synchrotron-based diffraction technique for in situ characterization of deformation behaviour in magnesium alloys, J. Appl. Crystallogr. **51**, 1082 (2018).

[51] F. Kabirian, A. S. Khan, and T. Gnäupel-Herlod, Visco-plastic modeling of mechanical responses and texture evolution in extruded AZ31 magnesium alloy for various loading conditions, Int. J. Plast. **68**, 1 (2015).

[52] J. Yao, B. Wang, L. Deng, A. Chapuis, Q. Li, and Q. Liu, Simulation of texture evolution and deformation mechanism in Mg-3Al-1Zn alloy during uniaxial compression, Sci. China Technol. Sci. **58**, 2052 (2015).

[53] D. Culbertson, Q. Yu, J. Wang, and Y. Jiang, Pre-compression effect on microstructure evolution of extruded pure polycrystalline magnesium during reversed tension load, Mater. Charact. **134**, 41 (2017).

[54] P. Chen, B. Li, D. Culbertson, and Y. Jiang, Contribution of extension twinning to plastic strain at low stress stage deformation of a Mg-3Al-1Zn alloy, Mater. Sci. Eng. A **709**, 40 (2018).